Supporting Information for "Isostatic equilibrium in spherical coordinates and implications for crustal thickness on the Moon, Mars, Enceladus, and elsewhere"

Douglas J. Hemingway,[1] and Isamu Matsuyama,[2]

Contents of this file

1. Text S1 to S3

2. Figures S1 to S7

Corresponding author: D. J. Hemingway, Department of Earth and Planetary Science, University of California, Berkeley, 94720, USA. (djheming@berkeley.edu)

[1]Department of Earth and Planetary

Science, University of California, Berkeley,

USA.

[2]Lunar and Planetary Laboratory,

University of Arizona, Tucson, Arizona,

USA.

S1. Internal Structure, Pressure, and Gravity

S1.1. Basic interior structure

Consider a simplified model for a planetary body consisting of N concentric spherical shells of different densities, with the requirement that the densities increase monotonically inward. The mean density, $\bar{\rho}$, of such a body is

$$\bar{\rho} = \sum_{i=1}^{N} \Delta\rho_i \left(\frac{R_i}{R}\right)^3 \tag{S1}$$

where R is the body's full radius, R_i is the radius of the ith layer, and $\Delta\rho_i$ is the density contrast between layer i and the layer above it.

If we relax the assumption of spherical symmetry, we can express the shape of the ith layer in terms of a spherical harmonic expansion as

$$H_i\left(\theta, \phi\right) = R_i + \sum_{l=1}^{\infty} \sum_{m=-l}^{l} H_{ilm} Y_{lm}\left(\theta, \phi\right) \tag{S2}$$

where θ and ϕ are the colatitude and longitude, respectively, $Y_{lm}\left(\theta, \phi\right)$ are the spherical harmonic functions for degree-l and order-m [e.g., *Wieczorek*, 2015], R_i is the mean radius of the ith layer, and where the coefficients H_{ilm} describe the departure from spherical symmetry for the ith layer.

S1.2. Internal pressure

The hydrostatic (or lithostatic) pressure at an arbitrary location within the interior is given by

$$p\left(r, \theta, \phi\right) = \int_{r}^{\infty} \rho\left(r', \theta, \phi\right) g\left(r'\right) dr' \tag{S3}$$

where $\rho\left(r', \theta, \phi\right)$ can be determined from the layer shapes, $H_i\left(\theta, \phi\right)$, given the assumption of uniform density within each layer (ρ_i), and where the radial component of the

gravitational acceleration is given by

$$g(r) = 4\pi G \frac{1}{r^2} \int_0^r \rho(r') r'^2 dr' \tag{S4}$$

where we neglect the small lateral variation in gravitational acceleration that arises because of the topography (H_{ilm}). For sufficiently simplified interior models, the internal hydrostatic pressure can be computed analytically by substituting (S4) into (S3) and integrating, as we have done in order to produce Figure 1 in the main text.

It will become useful to define the mean density below radius r as

$$\bar{\rho}_r = \frac{M(r)}{\frac{4}{3}\pi r^3} = \frac{3}{r^3} \int_0^r \rho(r') r'^2 dr' \tag{S5}$$

allowing us to express the gravitational acceleration as

$$g(r) = \frac{4}{3}\pi G r \bar{\rho}_r \tag{S6}$$

S1.3. Gravitational potential

The gravitational potential at an arbitrary location, following the convention of the potential being everywhere negative, is given by [e.g., *Hubbard*, 1984]

$$U(r, \theta, \phi) = -4\pi G \left(\frac{1}{r} \int_0^r \rho(r') r'^2 dr' + \int_r^R \rho(r') r' dr' \right) + \Delta U(r, \theta, \phi) \tag{S7}$$

where $\Delta U(r, \theta, \phi)$ represents the asymmetric part of the potential, and is given by

$$\Delta U(r, \theta, \phi) = U^{\text{rot}}(r, \theta, \phi) + U^{\text{tid}}(r, \theta, \phi) + \sum_{l=1}^{\infty} \sum_{m=-l}^{l} U_{lm}(r) Y_{lm}(\theta, \phi) \tag{S8}$$

where U^{rot} and U^{tid} are the laterally varying rotational and (if applicable) tidal potentials, respectively, given by

$$U^{\text{rot}}(r, \theta, \phi) = \omega^2 r^2 \left(-\frac{1}{3} + \frac{1}{3} Y_{20}(\theta, \phi) \right)$$

and (for a tidally locked satellite)

$$U^{\text{tid}}(r, \theta, \phi) = \omega^2 r^2 \left(\frac{1}{2} Y_{20}(\theta, \phi) - \frac{1}{4} Y_{22}(\theta, \phi) \right)$$

where ω is the spin period. The coefficients U_{lm} in (S8) account for the gravitation associated with the topography and thus depend on the layer shapes and densities (assumed uniform within each layer), and are given by

$$U_{lm}(r) = -\frac{4\pi Gr}{2l+1} \sum_{i=1}^{N} \Delta\rho_i H_{ilm} \begin{cases} \left(\frac{R_i}{r}\right)^{l+2} & r \geq R_i \\ \left(\frac{r}{R_i}\right)^{l-1} & r < R_i \end{cases} \tag{S9}$$

The gravitational potential exterior to the body $(r \geq R)$ can also be expressed as

$$U(r, \theta, \phi) = -\frac{GM}{r} \sum_{l=0}^{\infty} \sum_{m=-l}^{l} \left(\frac{R_{\text{ref}}}{r}\right)^l C_{lm} Y_{lm}(\theta, \phi) \tag{S10}$$

where M is the total mass of the body, and where C_{lm} are dimensionless gravitational potential coefficients, with $C_{00} = 1$ by definition, and with the other coefficients being obtained by evaluating (S9) at some reference radius, R_{ref}, and dividing by $-GM/R_{\text{ref}}$, yielding

$$C_{lm} = \frac{3}{2l+1} \left(\frac{R_{\text{ref}}^2}{\bar{\rho}R^3}\right) \sum_{i=1}^{N} \Delta\rho_i H_{ilm} \left(\frac{R_i}{R_{\text{ref}}}\right)^{l+2} \tag{S11}$$

where again, R is the body's mean radius, which in general may differ from the reference radius, R_{ref}. If $R_{\text{ref}} = R$, then

$$C_{lm} = \frac{3}{2l+1} \left(\frac{1}{\bar{\rho}R}\right) \sum_{i=1}^{N} \Delta\rho_i H_{ilm} \left(\frac{R_i}{R}\right)^{l+2} \tag{S12}$$

S1.4. Gravitational acceleration

In spite of the lateral variations in gravitational acceleration being small enough to neglect for purposes of computing the internal pressure, we are sometimes concerned with the magnitude of these small lateral variations, or gravity anomalies. These gravity

anomalies, evaluated at or above the surface $(r \geq R)$, can be obtained by differentiating

(S9) with respect to r to get the (positive downward) gravitational acceleration

$$g_{lm}(r) = \frac{l+1}{2l+1} 4\pi G \sum_{i=1}^{N} \Delta\rho_i H_{ilm} \left(\frac{R_i}{r}\right)^{l+2} \tag{S13}$$

When the potential is instead expressed in terms of the dimensionless potential coeffi-

cients, C_{lm}, the equivalent result is obtained by differentiating (S10) to get

$$g_{lm}(r) = (l+1) \frac{GM}{r^2} \left(\frac{R_{\text{ref}}}{r}\right)^{l} C_{lm} \tag{S14}$$

S1.5. Radial variation in gravity

As we showed in the main text, the radial variation in gravity is relevant to the iso-

static equilibrium problem and has implications for spectral admittance and gravity-to-

topography ratio (GTR) models. From (S6), it is clear that the ratio of the mean surface

gravity (g_t) to the mean gravity at the base of the crust (g_b) is

$$\frac{g_t}{g_b} = \frac{\bar{\rho} R_t}{\bar{\rho}_b R_b} \tag{S15}$$

where $\bar{\rho}$ is the body's mean density and $\bar{\rho}_b$ is the mean density of all the material below

the base of the crust. Using (S1), it can be further shown that, if the crustal density is

ρ_c, such that

$$\bar{\rho} = \rho_c + (\bar{\rho}_b - \rho_c) \left(\frac{R_b}{R_t}\right)^3 \tag{S16}$$

then

$$\frac{g_t}{g_b} = \frac{(R_b/R_t)^2}{1 + \left((R_b/R_t)^3 - 1\right) \frac{\rho_c}{\bar{\rho}}} \tag{S17}$$

The ratio g_t/g_b thus depends only on the relative compensation depth (d/R_t, where

$d = R_t - R_b$) and the internal density structure, the relevant part of which is effectively

captured in the ratio $\rho_c/\bar{\rho}$ (Figure S1).

S2. Airy vs Pratt Isostasy

In the main text, we focused on the case of Airy isostasy, wherein the topography is supported by buoyant roots at the base of the crust (Figure S2a). In Pratt isostasy, the topography is supported instead by lateral variations in crustal density (Figure S2b). The problem of modeling Pratt-type isostatic compensation can be framed as the need to compute the lateral variations in crustal density required to eliminate lateral pressure gradients at the depth of compensation ($d = R_t - R_b$). Given the known surface topography (h_t) and assuming a Cartesian geometry with constant gravity, we have

$$\rho_c g d = (\rho_c + \delta\rho) g (d + h_t) \tag{S18}$$

from which it follows that

$$\delta\rho = -\rho_c \left(\frac{h_t}{d + h_t} \right) \tag{S19}$$

Provided that $|h_t| \ll d$, we can linearize (S19) to obtain the more convenient expression

$$\delta\rho = -\rho_c \left(\frac{h_t}{d} \right) \tag{S20}$$

Whereas this Cartesian formulation is adequate in most cases, we wish to examine the effect of taking the spherical geometry into account. Here again we examine the two distinct conceptions of the condition of isostatic equilibrium in spherical coordinates: 1) the requirement of equal masses in columns of equal solid angle; and 2) the requirement of the absence of lateral pressure gradients at depth, where pressure is assumed to be hydrostatic. Figure S2b illustrates a cross section of a two-layer body having a crust with mean density ρ_c. The left hand side of the figure shows a part of the body with zero topography with respect to the mean radius R_t. The right hand side of the figure shows a

part of the body with some positive topographic anomaly at the top of the crust ($h_t > 0$) and a corresponding crustal density anomaly, $\delta\rho$.

S2.1. Equal Masses Pratt Isostasy

Equating the wedge mass in the absence of the topographic anomaly (left side of Figure S2b) with the wedge mass in the presence of the topographic anomaly (right side of Figure S2b), yields

$$\rho_c \int_{R_b}^{R_t} r^2 dr = (\rho_c + \delta\rho) \int_{R_b}^{R_t+h_t} r^2 dr$$

After integrating and some manipulation, and making use of a substitution for the crustal thickness ($d = R_t - R_b$), we obtain

$$\delta\rho \left(\frac{1}{3}\left(1 + \frac{R_b}{R_t} + \left(\frac{R_b}{R_t}\right)^2\right) d + \left(1 + \frac{h_t}{R_t} + \frac{h_t^2}{3R_t^2}\right) h_t \right) = -\rho_c \left(1 + \frac{h_t}{R_t} + \frac{h_t^2}{3R_t^2}\right) h_t$$

As long as $|h_t| \ll R_t$, we can say that

$$\delta\rho \approx -\rho_c \left(\frac{h_t}{\frac{1}{3}\left(1 + \frac{R_b}{R_t} + \left(\frac{R_b}{R_t}\right)^2\right) d + h_t} \right) \tag{S21}$$

As expected, this expression converges to the Cartesian equivalent, (S19), when the compensation depth is shallow (as $R_b \to R_t$).

Provided that $|h_t| \ll d$, we can again linearize (S21) to obtain

$$\delta\rho \approx -\rho_c \left(\frac{h_t}{d}\right) \left(\frac{3}{1 + \frac{R_b}{R_t} + \left(\frac{R_b}{R_t}\right)^2} \right) \tag{S22}$$

S2.2. Equal Pressures Pratt Isostasy

Equating the hydrostatic pressure in the absence of the topographic anomaly (left side of Figure S2b) with the hydrostatic pressure in the presence of the topographic anomaly

(right side of Figure S2b), in both cases evaluated at $r = R_d$, we obtain

$$\delta\rho \int_{R_b}^{R_t+h_t} g(r)\, dr = -\rho_c \int_{R_t}^{R_t+h_t} g(r)\, dr$$

Once again, if $|h_t| \ll R_t$, then over the small radial distance between R_t and $R_t + h_t$, the

integrand on the right hand side has a nearly constant value of g_t, so the right hand side of

this equation becomes $\approx -\rho_c g_t h_t$. The integral on the left hand side is less straightforward.

However, if we assume that the gravity varies linearly from a value of g_b at the base of the

crust to g_t at and near the top of the crust, then we can approximate this integral by a

trapezoidal region of width $d + h_t$ and starting and ending heights g_b and g_t, making the

left hand side of this equation $\approx \delta\rho \left(\frac{g_t+g_b}{2}\right)(d + h_t)$ (this approximation is good to within

2% as long as $\rho_c/\bar{\rho} > 0.3$ and $R_b/R_t > 0.8$). The result is

$$\delta\rho \approx -\rho_c \left(\frac{h_t}{d + h_t}\right)\left(\frac{2}{1 + \frac{g_b}{g_t}}\right) \tag{S23}$$

As expected, this expression likewise converges to the Cartesian equivalent, (S19), when

the gravity at the compensation depth is similar to the surface gravity (i.e., as $g_b \to g_t$).

Provided that $|h_t| \ll d$, we can linearize (S23) to obtain

$$\delta\rho \approx -\rho_c \left(\frac{h_t}{d}\right)\left(\frac{2}{1 + \frac{g_b}{g_t}}\right) \tag{S24}$$

Compared with the "equal pressures" condition, the "equal masses" condition always

overestimates the magnitude of the lateral density variations (Figure S3b).

S2.3. Implications under Pratt model

S2.3.1. Spectral Admittance under Pratt isostasy

Under the model of Pratt compensation, we must abandon the assumption of uniform

density within each layer, meaning that equation (S9) is no longer sufficient to describe

the asymmetries in the potential. If the non-hydrostatic topography is limited to the surface (H_{tlm}), and if the lateral density variations (ρ_{lm}) are confined to the outermost layer (the crust), and do not vary radially within that layer, then the asymmetries in the gravitational potential, evaluated at or above the surface ($r \geq R_t$), are given by

$$U_{lm}\left(r\right) = -\frac{4\pi Gr}{2l+1}\left(\left(\rho_{\mathrm{c}}+\rho_{lm}\right)H_{tlm}\left(\frac{R_t}{r}\right)^{l+2} + \rho_{lm}\int_{r'=R_b}^{R_t+H_{tlm}}\left(\frac{r'}{r}\right)^{l+2}dr'\right)$$

The first term represents the effect of the extra mass associated with the surface topography (H_{tlm}) and the second term represents the effect of the lateral density variations within the crust (ρ_{lm}). When the density variations are small compared with the mean crustal density ($\rho_{lm} \ll \rho_{\mathrm{c}}$) and when the surface relief is small compared with the mean crustal thickness ($H_{tlm} \ll R_t - R_b$), we can neglect the terms in ($\rho_{lm}H_{tlm}$), and this expression simplifies to

$$U_{lm}\left(r\right) = -\frac{4\pi Gr}{2l+1}\left(\rho_{\mathrm{c}}H_{tlm}\left(\frac{R_t}{r}\right)^{l+2} + \rho_{lm}\int_{r'=R_b}^{R_t}\left(\frac{r'}{r}\right)^{l+2}dr'\right) \quad \text{(S25)}$$

Differentiating (S25) with respect to r, we obtain the (positive downward) gravitational acceleration, which we evaluate at $r = R_t$ to get

$$g_{lm}\left(R_t\right) = \frac{l+1}{2l+1}4\pi G\left(\rho_{\mathrm{c}}H_{tlm} + \frac{R_t}{(l+3)}\left(1-\left(\frac{R_b}{R_t}\right)^{l+3}\right)\rho_{lm}\right)$$

Setting ρ_{lm} to the linearized expression in equation (S20), we then obtain

$$g_{lm}\left(R_t\right) = \frac{l+1}{2l+1}4\pi G\left(\rho_{\mathrm{c}}H_{tlm} - \frac{1}{(l+3)}\left(1-\left(\frac{R_b}{R_t}\right)^{l+3}\right)\left(\frac{\rho_{\mathrm{c}}H_{tlm}}{1-\frac{R_b}{R_t}}\right)\right)$$

from which it follows that the spectral admittance is

$$Z_l = \frac{l+1}{2l+1}4\pi G\rho_{\mathrm{c}}\left(1-\frac{1}{(l+3)}\left(\frac{1-\left(\frac{R_b}{R_t}\right)^{l+3}}{1-\frac{R_b}{R_t}}\right)\right) \quad \text{(S26)}$$

Using the "equal masses" equation (S22) instead yields

$$Z_l = \frac{l+1}{2l+1} 4\pi G \rho_c \left(1 - \frac{1}{(l+3)} \left(\frac{1 - \left(\frac{R_b}{R_t}\right)^{l+3}}{1 - \frac{R_b}{R_t}} \right) \left(\frac{3}{1 + \frac{R_b}{R_t} + \left(\frac{R_b}{R_t}\right)^2} \right) \right) \tag{S27}$$

Finally, the "equal pressures" equation (S24) leads to

$$Z_l = \frac{l+1}{2l+1} 4\pi G \rho_c \left(1 - \frac{1}{(l+3)} \left(\frac{1 - \left(\frac{R_b}{R_t}\right)^{l+3}}{1 - \frac{R_b}{R_t}} \right) \left(\frac{2}{1 + \frac{g_b}{g_t}} \right) \right) \tag{S28}$$

As with the case of Airy compensation (Figure 2), the "equal masses" model for Pratt

compensation underestimates the admittance (Figure S4) compared with the "equal pres-

sures" model. The discrepancy is especially pronounced at the lowest spherical harmonic

degrees (longest wavelengths) and when compensation depths are large. Compared with

the Airy model, admittances computed assuming a Pratt model increase more gradually,

both with increasing compensation depth (Figure S4a) and increasing spherical harmonic

degree (Figure S4b). That is, for a given spherical harmonic degree, a Pratt model will

require a larger compensation depth to produce the same admittance.

S2.3.2. Geoid-to-topography ratio (GTR) under Pratt isostasy

Evaluating (S25) at $r = R_t$, we obtain

$$U_{lm}(R_t) = -\frac{4\pi G R_t}{2l+1} \left(\rho_c H_{tlm} + \rho_{lm} \frac{R_t}{(l+3)} \left(1 - \left(\frac{R_b}{R_t}\right)^{l+3} \right) \right)$$

from which it follows that the dimensionless gravitational potential coefficients of (S10)

become

$$C_{lm} = \frac{3}{2l+1} \left(\frac{\rho_c}{R_t \bar{\rho}} \right) \left(H_{tlm} + \frac{\rho_{lm}}{\rho_c} \frac{R_t}{(l+3)} \left(1 - \left(\frac{R_b}{R_t}\right)^{l+3} \right) \right)$$

Assuming complete Pratt compensation, with the lateral density variations computed

according to equation (S20), the geoid-to-topography ratio, given by equations (14) and

(15), becomes

$$\text{GTR} = \sum_{l=l_{\min}}^{l_{\max}} W_l \left(\frac{3}{2l+1}\right) \left(\frac{\rho_c}{\bar{\rho}}\right) \left(1 - \frac{1}{(l+3)} \left(\frac{1 - \left(\frac{R_b}{R_t}\right)^{l+3}}{1 - \frac{R_b}{R_t}}\right)\right)$$

When the lateral density variations are computed according to the "equal masses" equation (S22), we have

$$\text{GTR} = \sum_{l=l_{\min}}^{l_{\max}} W_l \left(\frac{3}{2l+1}\right) \left(\frac{\rho_c}{\bar{\rho}}\right) \left(1 - \frac{1}{(l+3)} \left(\frac{1 - \left(\frac{R_b}{R_t}\right)^{l+3}}{1 - \frac{R_b}{R_t}}\right) \left(\frac{3}{1 + \frac{R_b}{R_t} + \left(\frac{R_b}{R_t}\right)^2}\right)\right)$$
$$\text{(S29)}$$

Finally, using instead the "equal pressures" equation (S24), we have

$$\text{GTR} = \sum_{l=l_{\min}}^{l_{\max}} W_l \left(\frac{3}{2l+1}\right) \left(\frac{\rho_c}{\bar{\rho}}\right) \left(1 - \frac{1}{(l+3)} \left(\frac{1 - \left(\frac{R_b}{R_t}\right)^{l+3}}{1 - \frac{R_b}{R_t}}\right) \left(\frac{2}{1 + \frac{g_b}{g_t}}\right)\right) \qquad \text{(S30)}$$

For reference, the dipole moment approximation [*Ockendon and Turcotte*, 1977; *Haxby and Turcotte*, 1978] gives

$$\text{GTR} = \left(\frac{3}{4}\right) \left(\frac{\rho_c}{\bar{\rho}}\right) \left(1 - \frac{R_b}{R_t}\right) \qquad \text{(S31)}$$

As with the case of Airy compensation, the "equal masses" model always underestimates the GTR, or equivalently, overestimates the compensation depth corresponding to a given measured GTR (Figure S5). The relative differences between the "equal masses", "equal pressures", and "dipole moment" models are similar under either Airy or Pratt isostasy. The most significant difference between the Airy and Pratt models is that the Pratt model gives much smaller (roughly half the magnitude) GTRs for any given compensation depth. Equivalently, for a given GTR, the Pratt model requires a significantly larger compensation depth.

S3. Applications

In the main text section 3.3, we discussed several examples of how crustal thickness estimates are affected when the "equal pressures" model for Airy isostatic equilibrium is adopted in place of the "equal masses" model.

S3.1. The Moon and Mars

Here we reproduce Figure 3a from *Wieczorek and Phillips* [1997], but with one additional curve, corresponding to the "equal pressures" model described by equation (19) (Figure S6a). We likewise reproduce Figure 1 from *Wieczorek and Zuber* [2004], again with the additional "equal pressures" curve (Figure S6b). In both cases, we compute the power spectra anew using more recent topography models—namely degree and order 2600 spherical harmonic models for the lunar and Martian topography (both available at markwieczorek.github.io, and ultimately sourced from LOLA and MOLA gridded data products available on NASA's planetary data system). While we also repeated the GTR computations from these and recent gravity models—namely the degree and order 420 GRAIL model for the Moon and the degree and order 120 MRO model for Mars (both available on NASA's planetary data system)—we did this only as a sanity check to ensure that our GTR values would be similar to those of *Wieczorek and Phillips* [1997] and *Wieczorek and Zuber* [2004]. Rather than attempting to reproduce the masks required to isolate the highland regions of interest in both cases, we simply used the highlands-only GTR values obtained by *Wieczorek and Phillips* [1997] and *Wieczorek and Zuber* [2004]. Whereas the GTRs for the nearside lunar highlands were given explicitly in *Wieczorek*

and Phillips [1997], we worked backwards from the reported crustal thickness estimates of *Wieczorek and Zuber* [2004] to obtain the GTRs for the Martian highlands.

S3.2. Enceladus

We can also compute admittance as a function of compensation depth for the case of Enceladus and compare it to the observed value (Figure S7). The observed degree-3 admittance [*Iess et al.*, 2014] of $14 \pm 2.8\,\text{mGal/km}$ suggests a compensation depth of of $30 \pm 6\,\text{km}$ when the "equal masses" model is used, but just $17 \pm 4\,\text{km}$ when the "equal pressures" model is used instead. This example serves to illustrate that, when the available gravity/topography data are limited to the lowest spherical harmonic degrees, the compensation depth estimate is extremely sensitive to the difference between "equal masses" and "equal pressures " isostasy.

References

Belleguic, V., P. Lognonné, and M. Wieczorek (2005), Constraints on the Martian lithosphere from gravity and topography data, *Journal of Geophysical Research*, *110*(E11), E11,005, doi:10.1029/2005JE002437.

Beuthe, M. (2008), Thin elastic shells with variable thickness for lithospheric flexure of one-plate planets, *Geophysical Journal International*, *172*(2), 817–841, doi: 10.1111/j.1365-246X.2007.03671.x.

Beuthe, M., A. Rivoldini, and A. Trinh (2016), Enceladus' and Dione's floating ice shells supported by minimum stress isostasy, *Geophysical Research Letters*, *43*, doi: 10.1002/2016GL070650.

Čadek, O., et al. (2016), Enceladus's internal ocean and ice shell constrained from Cassini gravity, shape and libration data, *Geophys. Res. Lett.*, *43*, doi:10.1002/2016GL068634.

Čadek, O., M. Běhounková, G. Tobie, and G. Choblet (2017), Viscoelastic relaxation of Enceladus's ice shell, *Icarus*, *291*, 31–35, doi:10.1016/j.icarus.2017.03.011.

Dahlen, F. A. (1982), Isostatic geoid anomalies on a sphere, *Journal of Geophysical Research*, *87*(B5), 3943–3947, doi:10.1029/JB087iB05p03943.

Hager, B. H. (1983), Global isostatic geoid anomalies for plate and boundary layer models of the lithosphere, *Earth and Planetary Science Letters*, *63*(1), 97–109, doi: 10.1016/0012-821X(83)90025-0.

Haxby, W. F., and D. L. Turcotte (1978), On Isostatic Geoid Anomalies, *Journal of Geophysical Research*, *83*(B11), 5473–5478.

Heiskanen, W., and F. Vening-Meinesz (1958), Historical development of the idea of isostasy, in *The Earth and Its Gravity Field*, pp. 124–146, McGraw-Hill, New York.

Hemingway, D., F. Nimmo, H. Zebker, and L. Iess (2013), A rigid and weathered ice shell on Titan, *Nature*, *500*(7464), 550–552, doi:10.1038/nature12400.

Hemingway, D. J., M. Zannoni, P. Tortora, F. Nimmo, and S. W. Asmar (2016), Dione's Internal Structure Inferred from Cassini Gravity and Topography, in *Lunar and Planetary Science Conference*, vol. 47, p. 1314.

Hubbard, W. B. (1984), *Planetary Interiors*, Van Nostrand Reinhold Company, New York.

Iess, L., N. J. Rappaport, R. A. Jacobson, P. Racioppa, D. J. Stevenson, P. Tortora, J. W. Armstrong, and S. W. Asmar (2010), Gravity field, shape, and moment of inertia of Titan., *Science (New York, N.Y.)*, *327*(5971), 1367–9, doi:10.1126/science.1182583.

Iess, L., et al. (2014), The Gravity Field and Interior Structure of Enceladus, *Science (New York, N.Y.)*, *344*(6179), 78–80, doi:10.1126/science.1250551.

Jeffreys, H. (1976), *The Earth: its origin, history, and physical constitution*, 6th ed., Cambridge University Press, New York.

Kraus, H. (1967), *Thin Elastic Shells*, Wiley, New York.

Lambeck, K. (1988), *Geophysical Geodesy: The Slow Deformations of the Earth*, Oxford University Press, New York.

Lambert, W. D. (1930), The form of the geoid on the hypothesis of complete isostatic compensation, *Bulletin géodésique*, *26*(1), 98–106.

McGovern, P. J., et al. (2002), Localized gravity/topography admittance and correlation spectra on Mars: Implications for regional and global evolution, *Journal of Geophysical Research*, *107*(E12), 1–25, doi:10.1029/2002JE001854.

McKenzie, D., F. Nimmo, J. A. Jackson, P. B. Gans, and E. L. Miller (2000), Characteristics and consequences of flow in the lower crust, *Journal of Geophysical Research*, *105*(B5), 11,029–11,046, doi:10.1029/1999JB900446.

McKinnon, W. B. (2015), Effect of Enceladus's rapid synchronous spin on interpretation of Cassini gravity, *Geophysical Research Letters*, *42*, doi:10.1002/2015GL063384.

Nimmo, F., B. G. Bills, and P. C. Thomas (2011), Geophysical implications of the long-wavelength topography of the Saturnian satellites, *Journal of Geophysical Research*, *116*(E11), E11,001, doi:10.1029/2011JE003835.

Ockendon, J. R., and D. L. Turcotte (1977), On the gravitational potential and field anomalies due to thin mass layers, *Geophysical Journal of the Royal Astronomical So-*

ciety, 48, 479–492.

Phillips, R. J., and K. Lambeck (1980), Gravity fields of the terrestrial planets: Long-wavelength anomalies and tectonics, *Review of Geophysics and Space Physics, 18*(1), 27–76.

Rambaux, N., F. Chambat, and J. C. Castillo-Rogez (2015), Third-order development of shape, gravity, and moment of inertia for highly flattened celestial bodies. Application to Ceres, *Astronomy & Astrophysics, 584*, A127, doi:10.1051/0004-6361/201527005.

Turcotte, D. L., R. J. Willemann, W. F. Haxby, and J. Norberry (1981), Role of Membrane Stresses in the Support of Planetary Topography, *Journal of Geophysical Research, 86*(1), 3951–3959.

Watts, A. B. (2001), *Isostasy and flexure of the lithosphere*, Cambridge University Press.

Wieczorek, M. (2015), Gravity and Topography of the Terrestrial Planets, in *Treatise on Geophysics*, 2nd ed., pp. 153–193, Elsevier B.V., doi:10.1016/B978-0-444-53802-4.00169-X.

Wieczorek, M. A., and R. J. Phillips (1997), The structure and compensation of the lunar highland crust, *Journal of Geophysical Research, 102*(E5), 10,933, doi:10.1029/97JE00666.

Wieczorek, M. A., and R. J. Phillips (1998), Potential anomalies on a sphere: Applications to the thickness of the lunar crust, *Journal of Geophysical Research, 103*(E1), 1715–1724.

Wieczorek, M. A., and M. T. Zuber (2004), Thickness of the Martian crust: Improved constraints from geoid-to-topography ratios, *Journal of Geophysical Research, 109*(E1),

1–16, doi:10.1029/2003JE002153.

Willemann, R. J., and D. L. Turcotte (1982), The role of lithospheric stress in the support

   of the Tharsis Rise, *Journal of Geophysical Research*, *87*(B12), 9793–9801.

Zhong, S. (1997), Dynamics of crustal compensation and its influences on crustal isostasy,

   Journal of Geophysical Research, *102*.

Zhong, S. (2002), Effects of lithosphere on the long-wavelength gravity anomalies and

   their implications for the formation of the Tharsis rise on Mars, *Journal of Geophysical*

   Research, *107*, doi:10.1029/2001JE001589.

Zhong, S., and M. T. Zuber (2000), Long-wavelength topographic relaxation for self-

   gravitating planets and implications for the time-dependent compensation of surface

   topography, *Journal of Geophysical Research*, *105*(E2), 4153–4164.
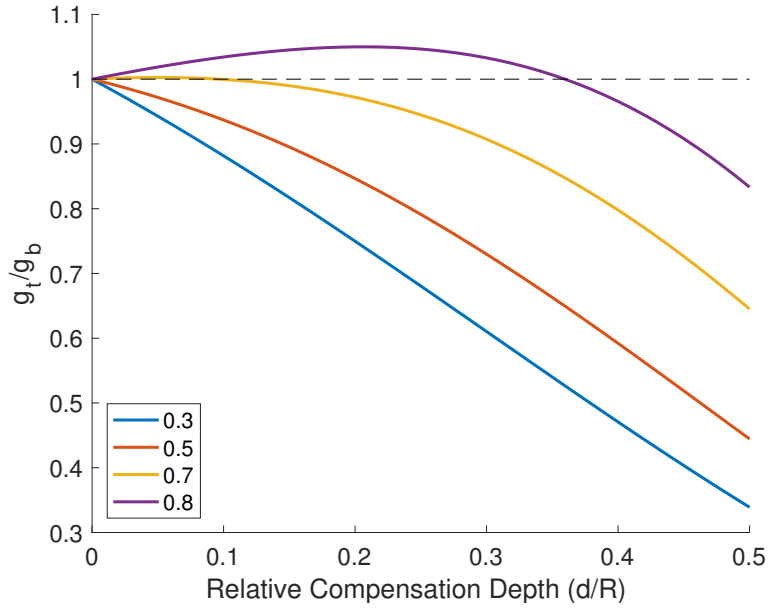
Figure S1.   Relationship between surface gravity (g_t) and the gravity at the base of

the crust (g_b) as a function of relative compensation depth $(d/R_t$, where $d = R_t - R_b)$,

for various internal density structures (described by the ratio of the crustal density to the
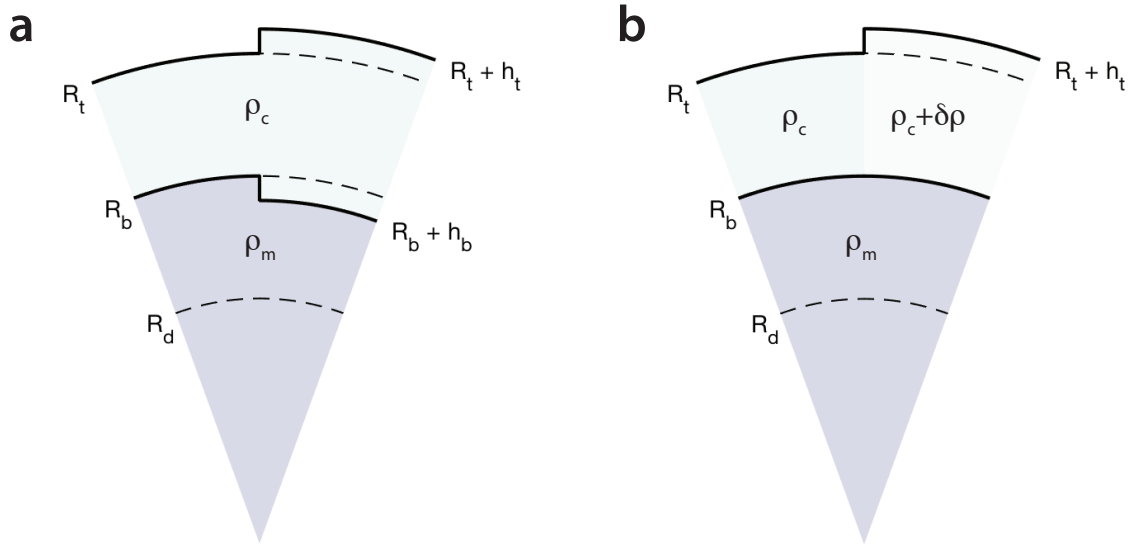
body's bulk density, $\rho_c/\bar{\rho})$.

Figure S2. Comparison of two hydrostatically supported wedges under the assumptions of Airy (a) and Pratt (b) isostatic equilibrium. In both cases, the left hand side of the figure shows a region having no topography with respect to the reference surface R_t, while on the right, there is a topographic anomaly of height h_t. In the Airy case (a), the topography is compensated by an accompanying isostatic root at the base of the crust. In the Pratt case (b), the nominal crustal density is ρ_c but the crust coinciding with the topographic anomaly has density $\rho_c + \delta\rho$ (when h_t is positive, $\delta\rho$ is negative).
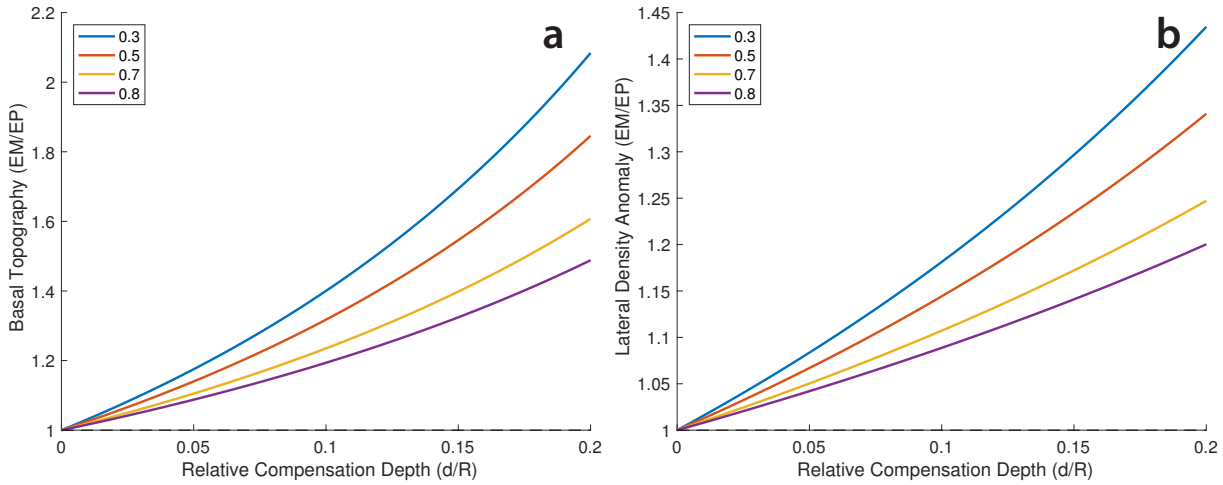
Figure S3. Comparison between "equal masses" (EM) and "equal pressures" (EP) isostasy models as a function of compensation depth and the body's internal density structure (characterized by the ratio $\rho_c/\bar{\rho}$). For Airy isostasy (a), this is the factor by which the amplitude of the basal topography is overestimated by the "equal masses" model. For Pratt isostasy (b), this is the factor by which the magnitude of the lateral density variations are overestimated by the "equal masses" model. The discrepancy becomes more pronounced with increasing compensation depth and with decreasing surface density to bulk density ratios ($\rho_c/\bar{\rho}$).
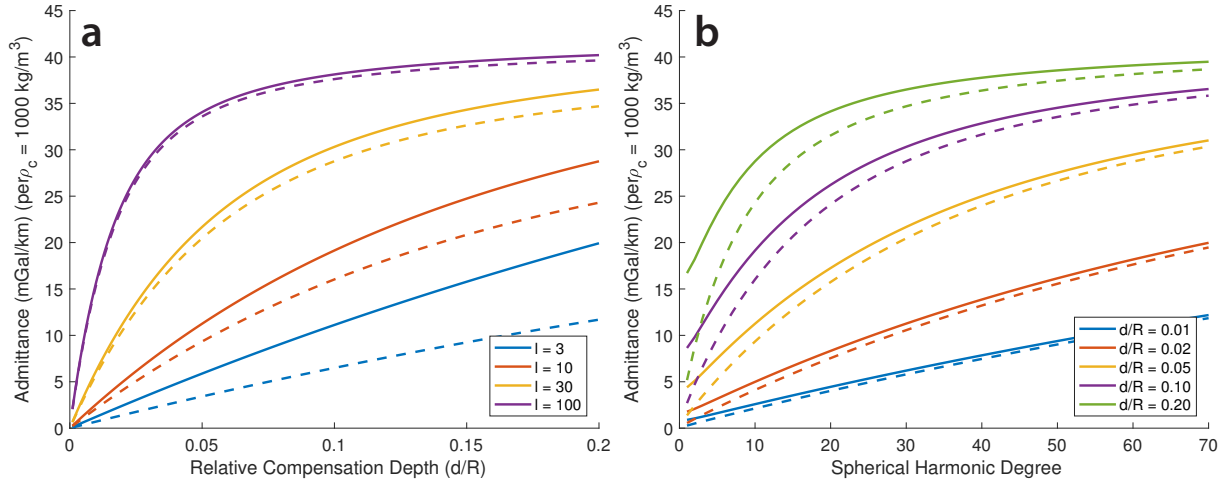
Figure S4. Admittance under Pratt isostasy. (a) Admittance as a function of relative compensation depth (d/R) for various example spherical harmonic degrees. (b) Spectral admittance for various examples of relative compensation depths. Dashed lines show admittance as computed via (S27), which assumes equal masses in equal columns. Solid lines show admittance as computed via (S28), which eliminates lateral pressure gradients at depth. The "equal masses" conception of isostasy always leads to underestimating the admittance, especially at low spherical harmonic degrees (long wavelengths). In both panels, admittance is normalized to an assumed crustal density of $1000\,\text{kg/m}^3$ (i.e., if the crustal density is $2000\,\text{kg/m}^3$, all admittance values double). Equation (S28) also depends weakly on the internal density structure, which is here arbitrarily defined by $\rho_c/\bar{\rho} = 0.6$. (*cf.* main text Figure 2.)
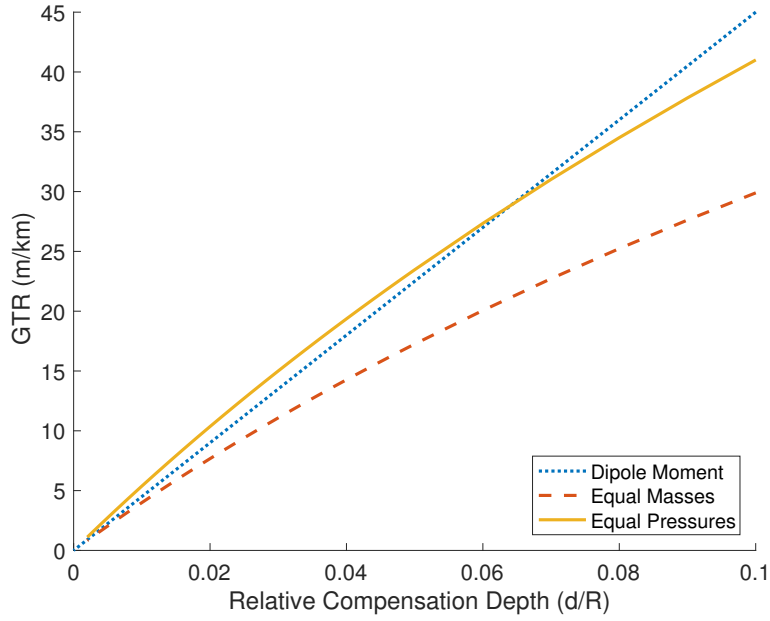
Figure S5. Geoid-to-Topography Ratio (GTR) as a function of relative compensation depth (d/R). Dotted blue line shows GTR computed via (S31), using the linear dipole moment approximation. Dashed red line shows GTR computed via (S29), which assumes equal masses in equal columns. Solid gold line shows GTR computed via (S30), which avoids lateral pressure gradients at depth. The internal density structure is again arbitrarily defined by $\rho_c/\bar{\rho} = 0.6$. The sum in (14) is taken from $l_{\min} = 3$ to $l_{\max} = 70$. The weighting coefficients are obtained from (16) by assuming a synthetic power spectrum defined by $S_{hh} = Al^{-1.5}$, where A is an arbitrary constant.
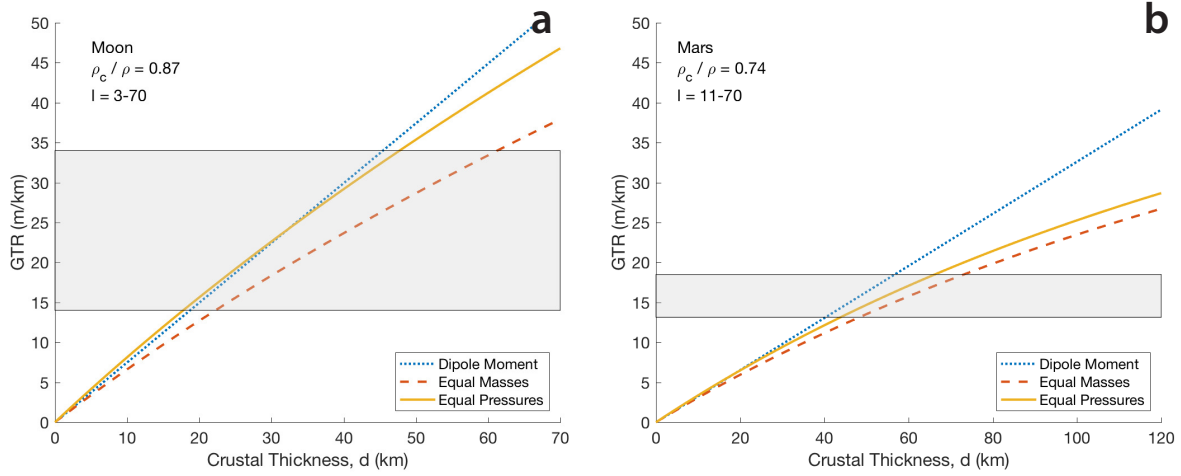
Figure S6. Geoid-to-Topography Ratio (GTR) as a function of crustal thickness. Dotted blue line shows GTR computed via (20), using the linear dipole moment approximation. Dashed red line shows GTR computed via (18), which assumes equal masses in equal columns. Solid gold line shows GTR computed via (19), which avoids lateral pressure gradients at depth. The grey bands represent the observed GTRs. Panel (a) represents the case of the nearside lunar highlands with $\rho_c = 2900 \, \text{kg/m}^3$ such that $\rho_c/\bar{\rho} \approx 0.87$, where the sum is taken from $l_{\min} = 3$ to $l_{\max} = 70$, and where the weighting coefficients are obtained using a power spectrum derived from a degree and order 2600 LOLA-based spherical harmonic model (*cf.* Figure 3a in *Wieczorek and Phillips* [1997]). Panel (b) represents the case of the Martian highlands with $\rho_c = 2900 \, \text{kg/m}^3$ such that $\rho_c/\bar{\rho} \approx 0.74$, where the sum is taken from $l_{\min} = 11$ to $l_{\max} = 70$ (*cf.* Figure 1 in *Wieczorek and Zuber* [2004]), and where we use a degree and order 2600 MOLA-based topography model.
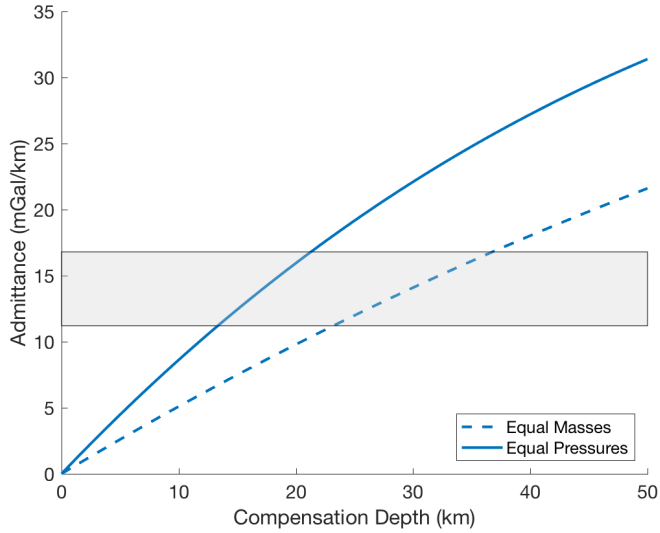
Figure S7.   Degree-3 admittance as a function of compensation depth for Enceladus.

Dashed line shows admittance as computed via (12), which assumes equal masses in equal

columns.   Solid line shows admittance as computed via (13), which eliminates lateral

pressure gradients at depth. Grey shaded region indicates degree-3 admittance obtained

from the observed gravity and topography [*Iess et al.*, 2014; *Nimmo et al.*, 2011].